α scattering and α-induced reaction cross sections of ^{64}Zn at low energies

A. Ornelas,[1] P. Mohr,[1,2] Gy. Gyürky,[1,*] Z. Elekes,[1] Zs. Fülöp,[1] Z. Halász,[1] G. G. Kiss,[1,†] E. Somorjai,[1] T. Szücs,[1]
M. P. Takács,[1,‡] D. Galaviz,[3,§] R. T. Güray,[4] Z. Korkulu,[4] N. Özkan,[4] and C. Yalçın[4]

[1]*Institute for Nuclear Research (MTA Atomki), H-4001 Debrecen, Hungary*
[2]*Diakonie-Klinikum, D-74523 Schwäbisch Hall, Germany*
[3]*Centro de Física Nuclear, University of Lisbon, 1649-003 Lisbon, Portugal*
[4]*Kocaeli University, Department of Physics, TR-41380 Umuttepe, Kocaeli, Turkey*

Background: α-nucleus potentials play an essential role for the calculation of α-induced reaction cross sections at low energies in the statistical model. Uncertainties of these calculations are related to ambiguities in the adjustment of the potential parameters to experimental elastic scattering angular distributions and to the energy dependence of the effective α-nucleus potentials.

Purpose: The present work studies the total reaction cross section σ_{reac} of α-induced reactions at low energies which can be determined from the elastic scattering angular distribution or from the sum over the cross sections of all open nonelastic channels.

Method: Elastic and inelastic ^{64}Zn$(\alpha,\alpha)^{64}$Zn angular distributions were measured at two energies around the Coulomb barrier, at 12.1 and 16.1 MeV. Reaction cross sections of the (α,γ), (α,n), and (α,p) reactions were measured at the same energies using the activation technique. The contributions of missing nonelastic channels were estimated from statistical model calculations.

Results: The total reaction cross sections from elastic scattering and from the sum of the cross sections over all open nonelastic channels agree well within the uncertainties. This finding confirms the consistency of the experimental data. At the higher energy of 16.1 MeV, the predicted significant contribution of compound-inelastic scattering to the total reaction cross section is confirmed experimentally. As a by-product it is found that most recent global α-nucleus potentials are able to describe the reaction cross sections for ^{64}Zn around the Coulomb barrier.

Conclusions: Total reaction cross sections of α-induced reactions can be well determined from elastic scattering angular distributions. The present study proves experimentally that the total cross section from elastic scattering is identical to the sum of nonelastic reaction cross sections. Thus, the statistical model can reliably be used to distribute the total reaction cross section among the different open channels.

I. INTRODUCTION

The nucleosynthesis of so-called *p*-nuclei on the neutron-deficient side of the chart of nuclides requires a huge reaction network including more than 1000 nuclei and more than 10 000 nuclear reactions (e.g., [1–4]). The resulting production factors depend sensitively on branchings between (γ,n) and (γ,α) reactions which are located several mass units "northwest" of stability on the chart of nuclides for heavy nuclei and close to stability for nuclei in the mass range around $A \approx 100$. It is impossible to measure all the required (γ,α) reaction rates in the laboratory. Instead, theoretical predictions have been used which are based on statistical model calculations. In most cases it turns out that the (γ,α) reaction rate is better constrained by experimental (α,γ) data than by (γ,α) data because of the strong influence of thermally excited states in the target nucleus [5–8].

Calculations of (γ,α) and (α,γ) cross sections and reaction rates depend on the α transmission which in turn depends on the chosen α-nucleus potential. Angular distributions of (α,α) elastic scattering have been measured with high precision in the past decade [9,10] to determine the α-nucleus potential at low energies. However, elastic scattering at low energies is dominated by the Coulomb interaction, and the angular distributions approach the Rutherford cross section for pointlike charges at astrophysically relevant energies. Consequently, α-nucleus potentials from elastic scattering are determined at somewhat higher energies and have to be extrapolated down to the astrophysically relevant energies.

It has turned out over the years that standard α-nucleus potentials like the extremely simple McFadden-Satchler potential [11] are able to reproduce (α,n) and (α,γ) cross sections around and above the Coulomb barrier, whereas at very low energies below the Coulomb barrier (i.e., in the astrophysically relevant energy range) an increasing overestimation of the experimental reaction cross sections has been found in many cases (e.g., [12–25]). Interestingly, in the $A \approx 20$–50 mass range, experimental (α,p) and (α,n) data are well described using the McFadden-Satchler potential [26]. Several alternative suggestions for low-energy α-nucleus potentials have been made in the past years [9,19,20,27–31], and the related

---

*gyurky@atomki.mta.hu

†Present address: RIKEN, 2-1 Hirosawa, Wako, Saitama 351-0198, Japan.

‡Present address: HZDR Dresden-Rossendorf, D-01314 Dresden, Germany.

§Present address: LIP Lisboa, 1000-149 Lisbon, Portugal.

uncertainties of α-induced reaction cross sections at low energies were studied very recently [32–34].

The motivation of the present work is manyfold. First, we attempt to extend the high-precision elastic scattering measurements of the past decade in the mass range $89 \leqslant A \leqslant 144$ [9] towards lower masses. Second, we include inelastic (α,α') scattering into our analysis, which may play a significant role for the total (nonelastic) reaction cross section σ_{reac} at very low energies [35,36]. Third, we have measured reaction cross sections of the (α,n), (α,p), and (α,γ) reactions at exactly the same energy as (α,α) elastic and inelastic scattering. This avoids any complications from the extrapolation of the energy-dependent α-nucleus potential. In our previous study [37] such experimental data were used for a sensitive test of the basic quantum-mechanical equation which relates the total reaction cross section σ_{reac} to the reflection coefficients η_L of elastic scattering. In the present work the reduced experimental uncertainties allow one to use the quantum-mechanical relation for σ_{reac} to constrain the cross sections of unobserved nonelastic channels. Note that the chosen target nucleus ^{64}Zn is well suited for such a study because most of the reaction products of α-induced reactions are unstable. This allows a simple and robust determination of the total cross section for each reaction channel by activation measurements.

The paper is organized as follows. In Sec. II we describe our experimental procedures for the measurement of α-induced reaction cross sections on ^{64}Zn and ^{64}Zn$(\alpha,\alpha)^{64}$Zn scattering. Section III presents the analysis of our new scattering data and further scattering data from the literature. A comparison between the total reaction cross sections σ_{reac} from scattering and from the sum of the individual reaction cross sections is given in Sec. IV. The predictions of recent global α-nucleus potentials are compared to our experimental reaction data in Sec. V. A final discussion and conclusions are provided in Sec. VI.

II. EXPERIMENTAL SETUP AND PROCEDURE

To give a comprehensive experimental description of the ^{64}Zn $+\alpha$ system, the cross sections of the following reaction channels were measured in the present work: The elastic α-scattering cross section at $E_\alpha = 12.1$ and 16.1 MeV was measured in a wide angular range. Inelastic scattering leading to the first four exited states of ^{64}Zn was also measured in an angular range limited to a more backward region. Using the activation technique, the cross sections of the ^{64}Zn$(\alpha,\gamma)^{68}$Ge, ^{64}Zn$(\alpha,n)^{67}$Ge, and ^{64}Zn$(\alpha,p)^{67}$Ga reactions were also measured at the same energies. Since the experimental techniques of both the scattering and activation experiments were already described in detail elsewhere [9,37], here only the most important features of the measurements and the results are presented.

A. Scattering experiments

The scattering experiments were carried out at the cyclotron accelerator of Atomki which provided α beams of 12.05 and 16.12 MeV energy with typical intensity of 150 nA. Targets
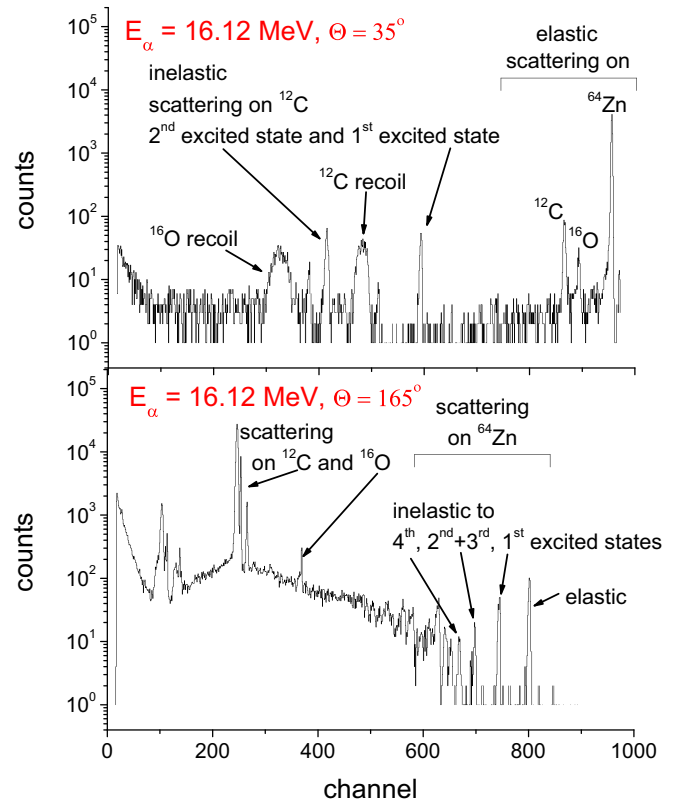

FIG. 1. Two typical scattering spectra measured at 16.12 MeV α energy at forward (35°, upper panel) and backward (165°, lower panel) angles. The origin of the most prominent peaks are indicated.

were produced by evaporating highly enriched (99.71%) metallic ^{64}Zn onto thin (40 μg/cm^2) carbon foils. The thickness of the ^{64}Zn layer was about 150 μg/cm^2 determined by α energy loss measurements. The energy loss at the energies of the scattering experiment is negligible compared to the energy width of the beam.

The angular distributions were measured in a scattering chamber equipped with seven ion-implanted Si particle detectors. The detectors were fixed on turntables enabling the measurement of scattered particle spectra in an angular range between 20° and 175°. In addition, two detectors were fixed at $\pm 15°$ with respect to the beam. These monitor detectors were used for normalization purposes. Two typical scattering spectra are shown in Fig. 1 recorded in the forward and backward regions, respectively. Peaks corresponding to elastic and inelastic scattering events on ^{64}Zn and on carbon and oxygen target components are indicated.

The elastic scattering cross sections were measured at both energies in the complete angular range between 20° and 175°. The excitation energies of the first four excited states of ^{64}Zn are 991.6 keV (2^+), 1799.4 keV (2^+), 1910.3 keV (0^+), and 2306.8 keV (4^+) [38,39]. The energy of the first excited state is far away enough from both the ground state and the higher-energy excited states so that the peak corresponding to the inelastic scattering leading to this excited state is well separated in the particle spectra. Therefore, the inelastic scattering cross section for this excited state could be

determined over a wider angular range. The only limitation is caused by the elastic scattering events on carbon and oxygen in the target which start to overlap with the inelastic peak in the forward angle region. Therefore, the inelastic scattering cross section to the first excited state could be only determined in the angular range between $40°$ and $175°$.

The second and third excited states could not be fully resolved because of their energy difference of about 100 keV. Therefore, only the sum of the cross sections leading to these states could be measured in the angular range between $60°$ and $175°$. Owing to the sufficient separation, the inelastic cross section leading to the fourth excited state could be determined from $60°$ to $175°$. Above the fourth exited state the level density becomes too high, and hence no further inelastic cross sections could be measured to higher-lying levels.

The experimental data will be provided to the community in tabular form through the EXFOR database [40].

B. Activation experiments

The activation cross-section measurements have been already carried out and published in full detail [37]. In the present work only one additional data point was determined since in Ref. [37] no measurement was carried out at 16.12 MeV α energy, which is one of the energies where the scattering cross section was measured in the present work and the total cross section σ_{reac} is determined.

The new measurement at 16.12 MeV α energy was carried out with exactly the same conditions as the experiments of [37]. The cyclotron accelerator provided the α beam which bombarded a thin natural isotopic composition Zn target on Al foil backing. The number of the ^{68}Ge, ^{67}Ge, and ^{67}Ga isotopes produced by the ^{64}Zn$(\alpha,\gamma)^{68}$Ge, ^{64}Zn$(\alpha,n)^{67}$Ge, and ^{64}Zn$(\alpha,p)^{67}$Ga reactions, respectively, was determined off-line by measuring the γ radiation following the decay of the reaction products with a shielded 100% relative efficiency HPGe detector.

Table I summarizes the results of the activation cross-section measurements. The first row at 12.05 MeV α energy is taken from [37] while the second one at 16.12 MeV is the result of the present work. The last column shows the sum of the cross sections of the three reactions. These values are used in the next sections for the determination of the total cross sections.

The energies $E_{\alpha,\mathrm{lab}}$ in the scattering experiments and in the activation experiments were identical because exactly the same settings for the cyclotron were used. At the higher energy of 16.1 MeV the effective energies of the scattering and activation experiments are the same ($E_{\mathrm{c.m.}} = 15.17$ MeV)

because relatively thin targets were used here. However, at the lower energy of 12.1 MeV a thicker target had to be used for the activation experiment leading to a slightly lower effective energy in the activation experiment ($E_{\mathrm{c.m.}}^{\mathrm{eff}} = 11.29$ MeV compared to $E_{\mathrm{cm.}} = 11.34$ MeV). The beam line for the scattering experiments allows a more precise measurement of the beam energy using the well-calibrated analyzing magnet in this beam line. Compared to the data in Ref. [37] ($E_{\mathrm{c.m.}}^{\mathrm{eff}} = 11.24 \pm 0.09$ MeV), this leads to a minor change of 50 keV in the effective energy for the 12.1-MeV activation experiment. This minor change remains within the given uncertainties of [37].

III. ANALYSIS OF SCATTERING DATA

In a first step, the new elastic scattering data at low energies together with data from literature are analyzed in the optical model (OM). Fortunately, several angular distributions of ^{64}Zn$(\alpha,\alpha)^{64}$Zn elastic scattering at higher energies are also available in the literature. Therefore, we can study the energy dependence of the angular distributions, the total reaction cross section σ_{reac}, and the resulting optical model potentials (OMPs). We restrict ourselves to data below about 50 MeV.

The complex OMP $U(r)$ is given by

$$U(r) = V(r) + iW(r) + V_C(r) \tag{1}$$

with the real part $V(r)$ and the imaginary part $W(r)$ of the nuclear potential and the Coulomb potential $V_C(r)$. The Coulomb potential is calculated as usual from the model of a homogeneously charged sphere with the Coulomb radius R_C. Various parametrizations were used for the nuclear potentials $V(r)$ and $W(r)$.

For the imaginary part $W(r)$, Woods-Saxon (WS) potentials of volume and surface type were applied:

$$W(r) = W_V f_V(x) + W_S \frac{df_S(x)}{dx} \tag{2}$$

with the Woods-Saxon function

$$f_i(x) = [1 + \exp(x)]^{-1}, \tag{3}$$

where $x = (r - R_i A_T^{1/3})/a_i$ and $i = S, V$. W_V and W_S are the strengths of the volume and surface imaginary potentials, R_i are the radius parameters, a_i the diffuseness parameters, and $A_T^{1/3} = 4$ for the target ^{64}Zn. Note that the maximum depth of a surface WS potential in the chosen convention in Eq. (3) is $W_S/4$. Following [9], at low energies below 25 MeV only a surface imaginary potential was used in combination with a

TABLE I. Cross section of the three measured reaction channels: The last column shows the sum of the cross sections of the three reactions where the calculation of the uncertainty takes into account the common systematic uncertainties. Details of the analysis can be found in Ref. [37], and the results in the first row are taken from Ref. [37].

E_α	$E_{\mathrm{c.m.}}^{\mathrm{eff.}}$	^{64}Zn$(\alpha,\gamma)^{68}$Ge	^{64}Zn$(\alpha,n)^{67}$Ge	^{64}Zn$(\alpha,p)^{67}$Ga	Sum
(MeV)	(MeV)		Cross section (mbarn)		
12.05	11.29 ± 0.09	2.42 ± 0.21	109 ± 12	255 ± 28	366 ± 40
16.12	15.17 ± 0.08	0.71 ± 0.14	240 ± 26	428 ± 50	668 ± 72

real folding potential. At the higher energies a combination of volume and surface Woods-Saxon potentials is necessary to obtain excellent fits to the experimental angular distributions.

The real part of the nuclear potential was either taken as a volume WS potential (similarly defined as above for the imaginary part) or calculated from a folding procedure. Two parameters λ for the strength and w for the width were used to adjust the folding potential $V_F(r)$ to the experimental data:

$$V(r) = \lambda \times V_F(r/w). \tag{4}$$

Obviously, the width parameter w should remain close to unity; otherwise, the folding procedure would become questionable. The strength parameter λ is typically around 1.1–1.4, leading to volume integrals per interacting nucleon pair $J_R \approx 320$–350 MeV fm^3 for heavy nuclei with a closed proton or neutron shell whereas slightly higher values have been found for lighter nuclei and nonmagic nuclei. Further details on the folding procedure and the chosen interaction can be found in Ref. [9].

The total (nonelastic) reaction cross section σ_{reac} is related to the elastic scattering angular distribution by

$$\sigma_{\text{reac}} = \sum_L \sigma_L = \frac{\pi}{k^2} \sum_L (2L + 1)\left(1 - \eta_L^2\right). \tag{5}$$

Here $k = \sqrt{2\mu E_{\text{c.m.}}}/\hbar$ is the wave number, $E_{\text{c.m.}}$ is the energy in the center-of-mass (c.m.) system, and η_L are the real reflection coefficients. These η_L and the scattering phase shifts δ_L define the angular distribution $(\frac{d\sigma}{d\Omega})(\vartheta)$ of elastic scattering, whereas σ_{reac} depends only on the η_L but is independent of the δ_L. The σ_L are the contributions of the Lth partial wave to the total reaction cross section σ_{reac} which show a characteristic behavior as discussed, e.g., in Refs. [21,41].

A. Elastic scattering data from literature

Elastic ^{64}Zn$(\alpha,\alpha)^{64}$Zn scattering has been studied in many experiments over a broad energy range. Here we focus on the data up to energies of about 50 MeV. The determination of an optical potential from angular distributions requires high-quality scattering data over the full angular range. A careful determination of the uncertainties is also mandatory because these uncertainties have a dramatic impact on the χ^2 minimization procedure. Therefore, we briefly review the status of the data from the literature as well as the availability and reliability of the data in the EXFOR database [40]. The data are compared to the theoretical angular distributions in Fig. 2. The obtained OMP parameters are listed in Table II.

Di Pietro *et al.* [42] primarily studied ^{64}Zn$(^6$He $,^6$He$)^{64}$Zn elastic scattering, and for comparison also the ^{64}Zn$(\alpha,\alpha)^{64}$Zn reaction was studied at $E_{\text{lab}} = 13.2$ MeV. The data cover a broad angular range but there are also two larger gaps around $\vartheta \approx 60°$ and $110°$. The data (including uncertainties) are available from the EXFOR database [40].

Robinson and Edwards [43] measured angular distributions at $E_{\text{lab}} = 14.99$, 17.94, and 18.99 MeV. The data cover a broad angular range from very forward ($\vartheta \approx 10°$) to backward angles around $\vartheta \approx 150°$. The data are not yet available at EXFOR, and therefore the data had to be read from Fig. 2 in Ref. [43]. The digitization was performed using a high-resolution medical scanner. However, the quality of the data is
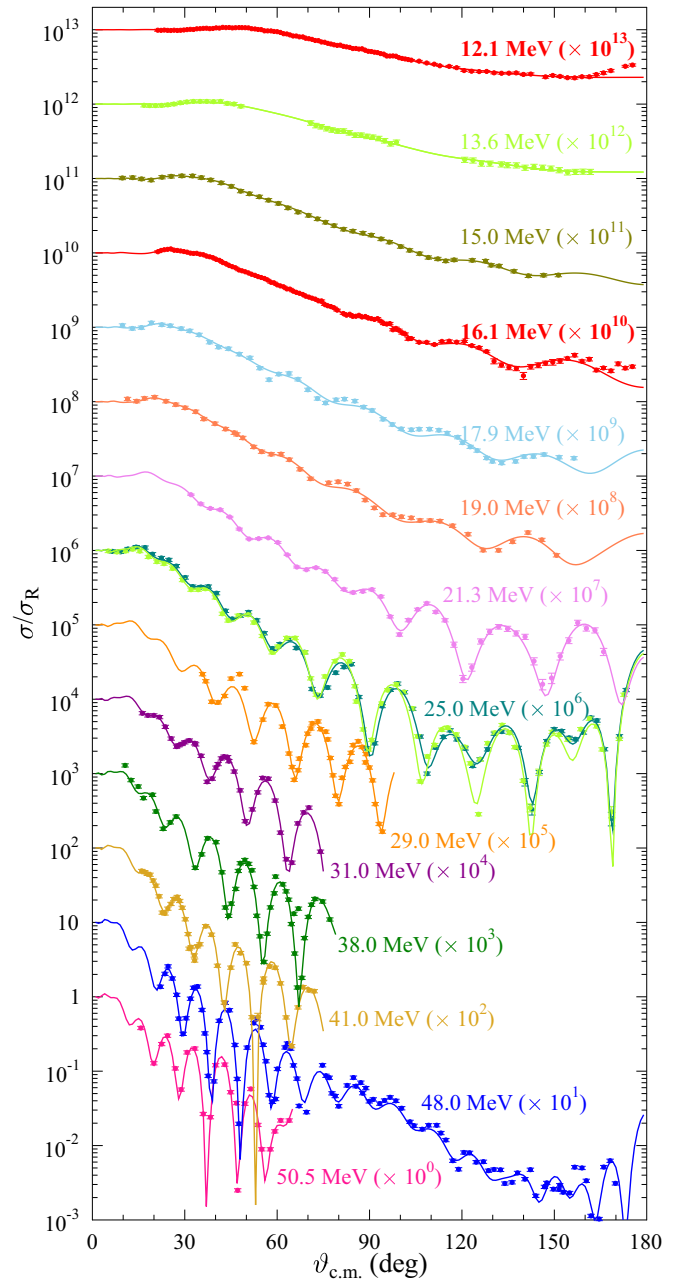

FIG. 2. Elastic ^{64}Zn$(\alpha,\alpha)^{64}$Zn scattering cross section at energies from 12 to 50 MeV. The new data at 12.1 and 16.1 MeV are shown in red and labeled in bold. The other experimental data are taken from Di Pietro *et al.* [42] (13.6 MeV), Robinson and Edwards [43] (15.0, 17.9, and 19.0 MeV), Fulmer *et al.* [44] (21.3 MeV), England *et al.* [45] and Ballester *et al.* [46] (25 MeV), Baktybaev *et al.* [47] (29, 38, and 50.5 MeV), Alpert *et al.* [49] (31 MeV), McDaniels *et al.* [50] (41 MeV), and Pirart *et al.* [52] (48 MeV).

essentially limited by the presentation of Fig. 2 in Ref. [43]. Error bars are typically smaller than the symbols in Fig. 2 of [43]; therefore, a fixed uncertainty of 5% has been assigned to all data points. Note that the chosen absolute value of 5% does affect the resulting χ^2/F but does not affect the χ^2 minimization procedure and the resulting OMP.

TABLE II. Parameters of the optical potential and the total reaction cross section $\sigma_{\rm reac}$ derived from $^{64}{\rm Zn}(\alpha,\alpha)^{64}{\rm Zn}$ angular distributions in the literature [42–47,49,50,52] and from this work (last two lines).

$E_{\rm lab}$ (MeV)	$E_{\rm c.m.}$ (MeV)	λ	w	J_R (MeV fm^3)	$r_{R,{\rm rms}}$ (fm)	W_V (MeV)	R_V (fm)	a_V (fm)	W_S (MeV)	R_S (fm)	a_S (fm)	J_I (MeV fm^3)	$r_{I,{\rm rms}}$ (fm)	N	$\sigma_{\rm reac}$[a] (mb)	Ref. Expt.
13.4	12.40	1.314	1.019	377.7	4.757				139.0	1.603	0.380	107.9	6.593	0.946	610 ± 80[b]	[42]
15.0	14.11	1.292	1.029	378.3	4.808				105.3	1.607	0.410	88.7	6.638	1.0[c]	858 ± 52	[43]
17.9	16.88	1.336	1.012	371.3	4.726				102.5	1.530	0.468	89.8	6.404	1.0[c]	1083 ± 65	[43]
19.0	17.87	1.344	1.015	377.9	4.744				111.0	1.525	0.456	94.1	6.371	1.0[c]	1149 ± 69	[43]
21.3	20.05	1.419	0.983	366.9	4.592	−24.0	1.233	0.895	−15.4	1.544	0.325	52.9	4.809	0.787	1327 ± 80	[44]
25.0	23.53	1.435	0.980	367.6	4.578	−32.9	1.080	0.985	−28.7	1.544	0.255	54.9	4.659	1.0[c]	1481 ± 89	[45]
25.0	23.53	1.457	0.986	379.9	4.605	−22.2	1.591	0.437	−79.0	1.478	0.302	59.6	4.565	1.0[c]	1317 ± 79	[46]
29.0	27.29	1.386	0.998	374.2	4.659	−2.5	1.963	0.338	214.3	1.245	0.336	109.0	5.369	1.344	1458 ± 88	[47]
31.0	29.17	1.353	0.995	362.3	4.646	−3.9	1.851	0.691	273.1	1.291	0.191	96.8	5.551	0.894	1608 ± 97	[49]
38.0	35.76	1.419	1.010	397.7	4.717	−10.6	1.816	0.339	322.4	1.318	0.062	95.1	5.628	0.920	1580 ± 95	[47]
41.0	38.58	1.384	0.972	345.2	4.537	−1.8	2.156	0.662	209.2	1.242	0.352	110.5	5.568	0.768	1797 ± 108	[50]
48.0	45.17	1.472	0.989	381.7	4.618	−28.5	1.532	0.603	−16.6	1.412	0.374	107.5	5.189	1.135	1691 ± 102	[52]
50.5	47.52	1.375	0.990	363.1	4.624	−4.3	1.961	0.419	204.8	1.267	0.178	80.9	5.640	1.608	1721 ± 103	[47]
12.1	11.34	1.288	1.038	394.5	4.845				186.5	1.697	0.275	116.6	6.876	1.0[c]	428 ± 7[d]	[e]
16.1	15.17	1.330	1.006	371.2	4.696				93.7	1.542	0.457	81.3	6.439	1.0[c]	905 ± 18[d]	[e]

[a]From the local potential fit using Eq. (5); uncertainties estimated as discussed in the text.
[b]Uncertainty from [37].
[c]Fixed normalization N.
[d]Discussion of uncertainty: see text.
[e]This work.

The data of Fulmer *et al.* [44] at $E_{\rm lab} = 21.3$ MeV are available in tabular form (Table V of [44]). The data reach the backward angular range up to $\vartheta \approx 165°$. However, the data unfortunately do not cover the forward region ($\vartheta \geqslant 32°$), and thus the absolute normalization cannot be fixed in the usual way by Rutherford scattering. Here it is interesting to note that a much better description of the experimental data can be obtained as soon as the absolute normalization of the data is considered as a free parameter. The best fit is obtained using a normalization of 0.787 for the data in Table V of [44]. Nevertheless, the resulting parameters of the fits do not change dramatically; i.e., already the shape of the angular distribution is able to constrain the fit reasonably well. For completeness it should also be mentioned that the data shown in Fig. 4 of [44] are also about 10% lower than the values given in Table V of [44].

There are two data sets at $E_{\rm lab} = 25$ MeV in EXFOR which reference England *et al.* [45] and Ballester *et al.* [46]. Both data sets were digitized from the given figures in Refs. [45,46] (Fig. 2 of [45] and Fig. 3 of [46]). The focus of [46] is inelastic scattering, and it is explicitly stated that "The elastic scattering data have already been published[30]." where the superscript "30" is a reference to [45]. Thus, both data sets should be identical. However, due to uncertainties of the digitization process, in fact both data sets show minor discrepancies (and not even the number of data points agree). We have decided to analyze both data sets; such an analysis can provide some insight into the uncertainties of the resulting OMP parameters which result from the redigitization procedure. The angular distribution published in Refs. [45,46] covers the full angular range from forward angles ($\vartheta \approx 10°$) to backward angles ($\vartheta \approx 170°$) with small uncertainties (typically smaller than

the shown point size). Unfortunately, these small uncertainties are not available anymore, and a fixed uncertainty of 5% was used in the fitting procedure. It turns out that the resulting OMP parameters from the two EXFOR data sets are close to each other. As with the analysis of the 21.3-MeV data (see discussion below), small discrepancies in the shape of the imaginary potential at large radii ($R \gtrsim 8$ fm) lead to noticeable effects in the total reaction cross section $\sigma_{\rm reac}$ which changes by about 10% from 1317 mb from the data of [46] to 1481 mb from the data of [45]. Therefore, we recommend the average $\sigma_{\rm reac} = 1399 \pm 82$ mb at 25 MeV, and we assign the same 6% uncertainty to all $\sigma_{\rm reac}$ data which are derived from digitized angular distributions.

The angular distributions at $E_{\rm lab} = 29$, 38, and 50.5 MeV measured by Baktybaev *et al.* [47] cover only a limited angular range up to about $\vartheta \approx 90°$. The data are available at EXFOR but have larger uncertainties of about 5–10%, which are further increased by the redigitization. Consequently, potentials derived from these data are not as reliable as in the other cases of this work. Further data from the same institute [48] are available at EXFOR. But these data [48] contain only very few points and are thus not included in the present analysis.

The data at 31 MeV by Alpert *et al.* [49] also cover only a limited angular range. The above statements on the Baktybaev *et al.* data also hold here. As the data are not available at EXFOR, we have redigitized the angular distribution from Fig. 3 of [49]. Error bars are not visible in this Fig. 3. We have used a fixed 5% uncertainty in the fitting procedure.

A limited angular distribution is available by McDaniels *et al.* [50] at 41 MeV. Redigitized data without uncertainties are available at EXFOR. Again we have used a
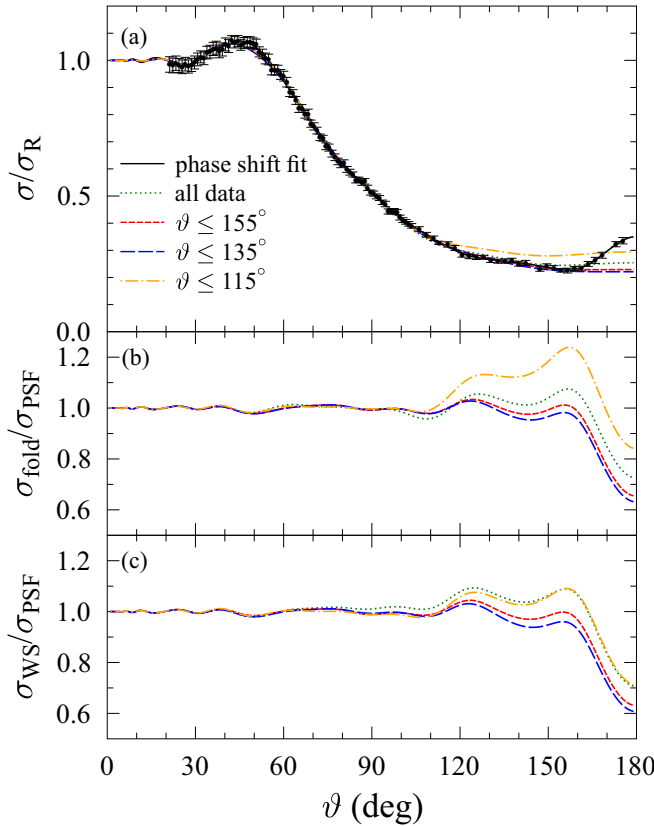
FIG. 3. (a) Elastic ^{64}Zn$(\alpha,\alpha)^{64}$Zn scattering cross section at $E =$ 12.1 MeV, compared to a phase shift analysis (PSF; solid black line) and to OM fits using a real folding and an imaginary surface Woods-Saxon potential. The fits use the full data set (green dotted line) and restricted data sets with $\vartheta \lesssim 155°$ (red dashed line), $\vartheta \lesssim 135°$ (blue long-dashed line), and $\vartheta \lesssim 115°$ (orange dash-dotted line). (b) OM fits normalized to the PSF, and (c) OM fits using volume Wood-Saxon potentials, again normalized to the PSF. For further discussion see text.

fixed 5% uncertainty for the fitting procedure of these data.

The data at 43 MeV by Broek *et al.* [51] cover a very limited angular range from about 10° to 50°. In addition, the scanned pages of this article (as provided at the ScienceDirect web page) are distorted. We decided to exclude these data from our analysis.

An excellent angular distribution at 48 MeV from about 20° to 170° is available from Pirart *et al.* [52]. Unfortunately, again the data in EXFOR had to be redigitized from Fig. 1 of [52] where uncertainties are not visible. Similar to the previous cases, we used a fixed 5% uncertainty in our analysis.

For all angular distributions, fits were performed in the following way. First, a folding potential was calculated at the average energy of 21.3 MeV using the energy-dependent parameters of the nucleon-nucleon interaction listed in Ref. [9]. The energy dependence of these parameters is relatively weak and has practically no impact on the final results. For a detailed discussion, see [9]. Next, the strength parameter λ and the width parameter w of the folding potential and the parameters

W_i, R_i, and a_i of the imaginary part were fitted simultaneously to the experimental angular distributions. In addition, the absolute normalization N of the angular distributions was allowed to vary because this absolute normalization often has much larger uncertainties. The normalization factors N deviate from unity by not more than about 30%. Fits with fixed $N = 1.0$ lead in many cases to much poorer χ^2 of the fit. For example, in the case of the 21.3-MeV data of Fulmer *et al.* [44], χ^2 reduces by about a factor of 4 from fixed $N = 1.0$ to fitted $N = 0.787$. The resulting OMP parameters remain relatively stable with variations of about 2% for the volume integrals J_R and J_I. However, relatively small changes in the shape of the imaginary potential at large radii ($R \gtrsim 8$ fm) result in a change of the total reaction cross section σ_{reac} of about 10% from 1200 mb for fixed $N = 1.0$ to 1327 mb for fitted $N = 0.787$. In cases where the additional free parameter N did not improve the reduced χ^2/F, a fixed normalization $N = 1.0$ was used. The results of these fits are shown in Fig. 2 and listed in Table II. In general, an excellent reproduction of the experimental angular distributions could be achieved in the full energy range under study. Further information on the uncertainties of the total reaction cross section σ_{reac} from elastic scattering angular distributions is given in Ref. [53].

B. New elastic scattering data at 12 and 16 MeV

After the successful description of the elastic ^{64}Zn$(\alpha,\alpha)^{64}$Zn scattering data from the literature [42–47,49,50,52], we expected a similar behavior for the analysis of our new data at 12.1 and 16.1 MeV. However, the new data cover backward angles up to about $\vartheta \approx 175°$, which exceeds the angular range of the literature data at low energies [42,43]. We found an unexpected increase of the Rutherford-normalized cross section which is more pronounced at the lower energy, and as it turns out it is practically impossible to describe the full angular distributions using an OMP composed of a real folding potential and an imaginary surface WS potential (similar to the fits to literature data at low energies). The reduced χ^2/F of the OM fits does not reach values around 1.0, but remains at about 2.0 (2.4) for the 12-MeV (16-MeV) data.

Therefore, we performed a phase shift fit (PSF) using the method of [54]. The PSFs are able to reproduce the full angular distributions at both energies with $\chi^2/F \lesssim 1$ (see Figs. 3 and 4). Values of $\chi^2/F \gg 1$ in a PSF would have been an indication for experimental problems.

The comparison between the OM fits and the PSFs shows clearly that the poor description of the angular distributions in the OM fits is related to the rise of the elastic scattering cross section at extreme backward angles. Therefore, we made additional fits which are restricted to data at $\vartheta \lesssim 155°$ (135°, 115°). Already the restriction to $\vartheta \lesssim 155°$ leads to a dramatic improvement of χ^2/F at both energies by about a factor of 2, whereas the χ^2/F do not improve further for the fits restricted to 135° or 115°. Therefore, we list the results for the OM fits truncated at $\vartheta = 155°$ in Table II.

Although the χ^2/F of the various fits differ significantly, it is difficult to visualize the differences. In the standard presentation (upper parts of Figs. 3 and 4) the various fits
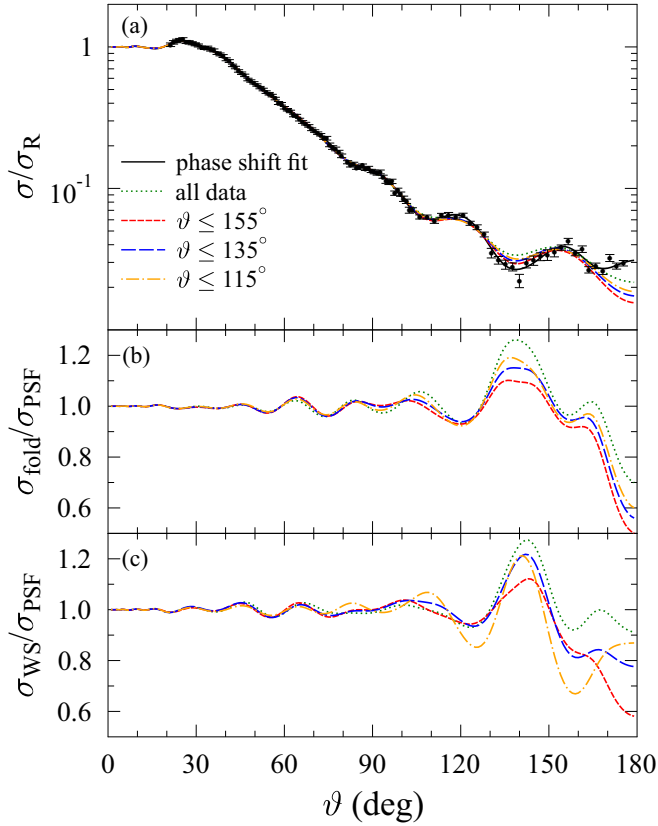
FIG. 4. Same as Fig. 3, but for the angular distribution at $E = 16.1$ MeV.

FIG. 5. Phase shifts δ_L, reflection coefficients η_L, and contribution σ_L of the Lth partial wave to σ_{reac} in Eq. (5) at $E_{\text{lab}} = 12.05$ MeV for the OMP fits using a folding potential in the real part and a surface WS potential in the imaginary part (from bottom to top). For further discussion see text.

are mostly hidden behind the experimental data. Therefore, we consider the PSFs (with $\chi^2/F \lesssim 1$) as quasi-experimental data and show the ratio between the OMP fits and the PSFs in the middle part of Figs. 3 and 4. Here it is nicely visible that all truncated fits underestimate the most backward cross sections by about 30–40%. As soon as the full data set is used for fitting, the underestimation at most backward angles becomes smaller (about 15–20%). However, at the same time the data between $120°$ and $160°$ are overestimated by about 10–20%; this leads to the overall significantly worse χ^2/F in this fit.

A relatively poor fit with $\chi^2/F \gg 1$ may also result from an inappropriate OMP. Although it is very unlikely that the otherwise successful folding potential [9] fails in the particular case of ^{64}Zn at low energies, we have repeated the above procedure of fitting the full angular distribution and truncated angular distributions using WS potentials of volume type in the real and imaginary part of the OMP. Almost exactly the same behavior was found in this case (see lower parts of Figs. 3 and 4).

From all the above calculations the total reaction cross sections were determined using Eq. (5). Fortunately, the results for σ_{reac} turn out to be very stable. At the lower energy we find an average value of $\sigma_{\text{reac}} = 428 \pm 7$ mb. The highest (lowest) value of $\sigma_{\text{reac}} = 440$ mb (420) is found for the folding potential truncated at $135°$ ($115°$). At the higher energy we find an average value of $\sigma_{\text{reac}} = 911 \pm 13$ mb. The highest (lowest) value of $\sigma_{\text{reac}} = 928$ mb (895) is found for the
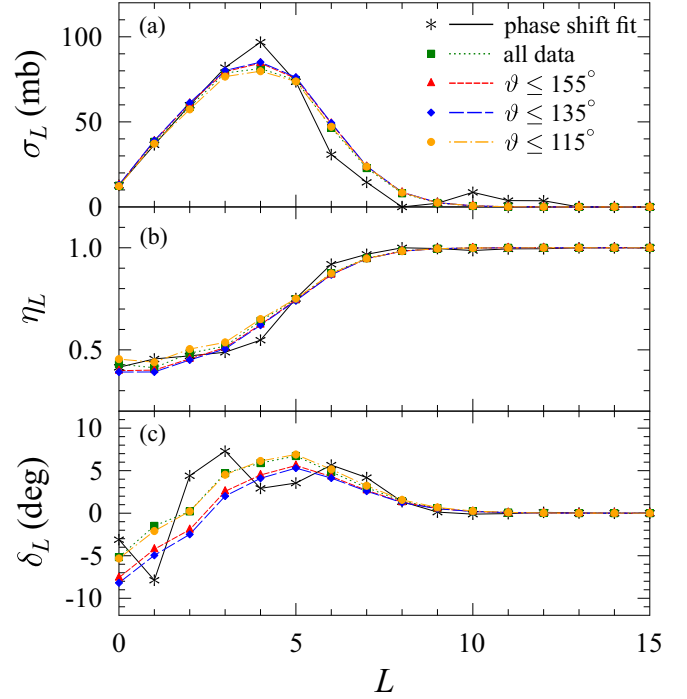
folding potential truncated at $155°$ (WS potential truncated at $135°$). The result of the PSF ($\sigma_{\text{reac}} = 898$ mb) is relatively close to the lowest result, and there seems to be a small systematic deviation between the folding potential fits (average $\sigma_{\text{reac}} = 925 \pm 3$ mb) and the WS potential fits (average $\sigma_{\text{reac}} = 902 \pm 5$ mb). Therefore, we recommend $\sigma_{\text{reac}} = 905 \pm 18$ mb (with a slightly increased 2% uncertainty) at the higher energy.

For a better understanding of the differences between the PSFs and the OMP fits we show the reflection coefficients η_L and the real phase shifts δ_L at both energies in Figs. 5–8.

At the lower energy of 12.1 MeV, there is an obvious discrepancy between the PSF and the OMP fits. The OMP fits lead to a relatively smooth variation of the phase shifts δ_L with the angular momentum number L. Contrary to the OMP fits, the PSF shows stronger variations in η_L and δ_L which cannot be reproduced by a typical α-nucleus potential. It is interesting to note that, although the underlying reflection coefficients η_L are not identical, the resulting total reaction cross section σ_{reac} is almost the same for all fits (see above).

At the higher energy of 16.1 MeV the discrepancies between the η_L and δ_L from the PSF and from the OMP fits are smaller. This is not surprising as the backward rise at the higher energy is not as pronounced as at 12.1 MeV. The small systematic discrepancy between the OMP fits using either a folding potential or a WS potential is mainly related to tiny differences in η_L for $8 \leqslant L \leqslant 11$.
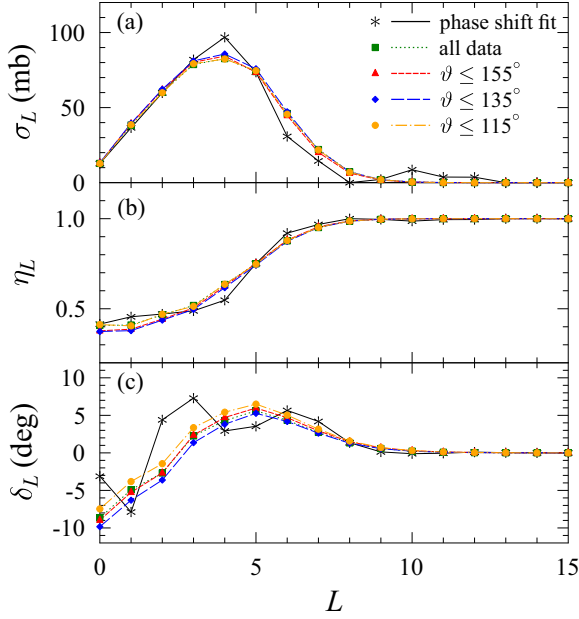
FIG. 6. Same as Fig. 5, but for the OMP fits with a volume WS potential in the real and imaginary part of the nuclear potential. For further discussion see text.

C. Reduced reaction cross section σ_{red}

Total reaction cross sections σ_{reac} of α-induced reactions for many target nuclei and in a broad energy range follow a systematic behavior which becomes visible in a plot of so-called reduced cross sections σ_{red} versus reduced energy E_{red} as suggested in Ref. [55]:

$$E_{\text{red}} = \frac{\left(A_P^{1/3} + A_T^{1/3}\right)E_{\text{c.m.}}}{Z_P Z_T}, \tag{6}$$
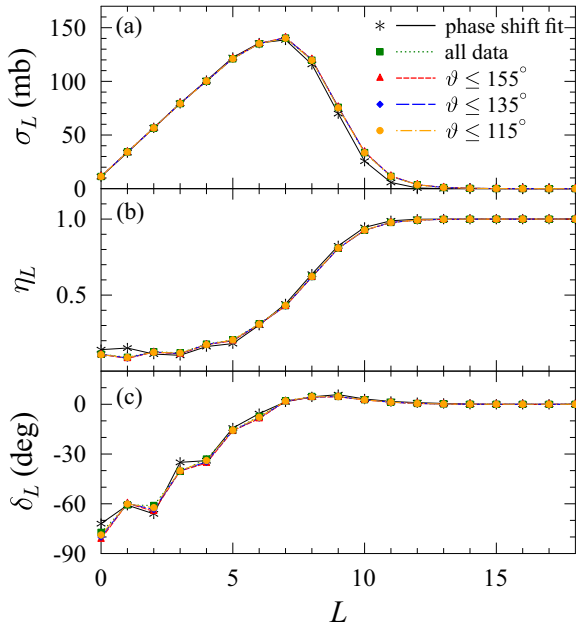

FIG. 7. Same as Fig. 5, but at $E_{\text{lab}} = 16.12$ MeV. For further discussion see text.
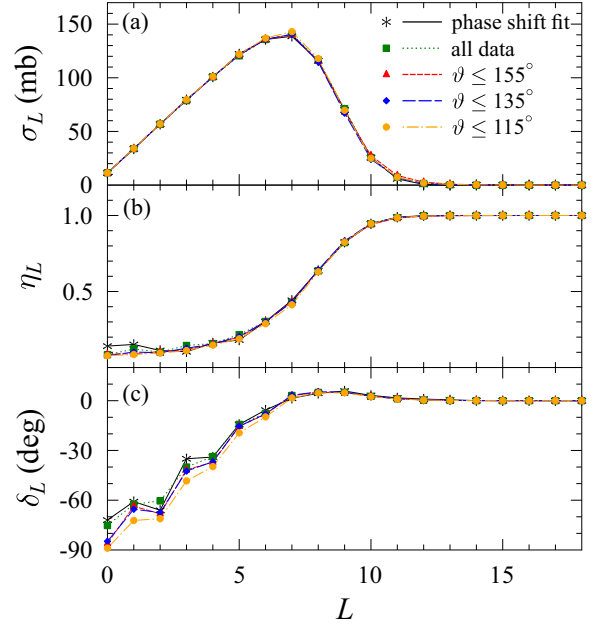

FIG. 8. Same as Fig. 7, but for the OMP fits with a volume WS potential in the real and imaginary parts of the nuclear potential. For further discussion see text.

$$\sigma_{\text{red}} = \frac{\sigma_{\text{reac}}}{\left(A_P^{1/3} + A_T^{1/3}\right)^2}. \tag{7}$$

The result is shown in Fig. 9. Contrary to the common trend for all nuclei with masses above $A \approx 90$, the data for ^{64}Zn are slightly higher than the general trend at all energies under study. Very recently, the analysis of reaction data for lighter targets (^{23}Na [56] and ^{33}S [57]) has shown that σ_{red} for these light nuclei is dramatically higher than the general trend
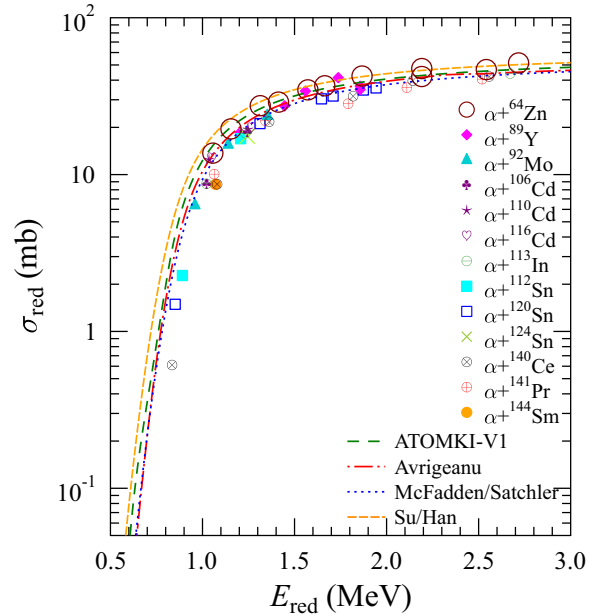

FIG. 9. Reduced reaction cross sections σ_{red} versus reduced energy E_{red} for various targets in a broad energy range. Except for ^{64}Zn, the data are taken from [9,21,41,63].

for heavy nuclei [58]. However, the dramatically increased reduced cross sections for ^{23}Na from the ^{23}Na$(\alpha,p)^{26}$Mg data of [56] were not confirmed by later experiments [59,60] and turned out to be an experimental error [61]. Figure 9 shows also the predictions from four α-nucleus potentials [9,11,19,27]. These results are discussed later.

For completeness it should be noted that there is an approximate relation between reduced energies and the Gamow window [62]: $E_{\mathrm{red},0} \approx 0.284$ MeV $\times T_9^{2/3}$. Consequently, the astrophysically relevant range for the reduced energy E_{red} is located below the shown range of Fig. 9 which was chosen from the availability of experimental scattering data.

D. ALAS for ^{64}Zn?

Anomalous large-angle elastic scattering (ALAS) was discussed in the literature already many years ago (e.g., [64,65]). However, there is no strict definition for ALAS. The phenomenon was first discussed in connection with ^{16}O$(\alpha,\alpha)^{16}$O and ^{40}Ca$(\alpha,\alpha)^{40}$Ca elastic scattering. For these reactions it was noticed later that the so-called anomalous cross sections are related to weak absorption of the doubly-magic target nuclei, and it is possible to describe the angular distributions within the OM [64–69]. Contrary to these findings, it turned out that the reproduction of the backward angular range in, e.g., ^{6}Li$(\alpha,\alpha)^6$Li or ^{20}Ne$(\alpha,\alpha)^{20}$Ne remains extremely difficult, and various explanations for the backward rise have been suggested: inelastic coupling to low-lying excited states, compound-elastic contributions, elastic α transfer, and angular-momentum-dependent absorption (e.g., [70–73]).

As we saw above, fortunately the influence of the backward rise on the derived total cross section σ_{reac} remains small. Therefore, a complete theoretical analysis of the backward rise remains beyond the scope of the present paper. Nevertheless, two of the above effects will be analyzed in more detail. First, inelastic scattering may contribute significantly to the total reaction cross section σ_{reac}. For a quantitative analysis we have measured several angular distributions (see Sec. III E). Second, compound-elastic scattering may contribute to the elastic scattering angular distribution but by definition it is not included in the OM analysis (see Sec. III F).

E. Analysis of inelastic scattering

One focus of the present study is the comparison between the total reaction cross section σ_{reac} from elastic scattering in Eq. (5) and the sum over all open nonelastic channels. This is discussed in further detail in Sec. IV. In addition to the real reaction channels like (α,n), (α,p), and (α,γ), inelastic (α,α') may contribute to this sum. In our previous study [37] we estimated the (α,α') cross section from coupled-channel calculations and from Coulomb excitation. Now we are able to provide experimental constraints for the (α,α') cross section for the low-lying states.

A precise experimental determination of the total (α,α') cross section is very difficult for at least two reasons. The total inelastic (α,α') cross section is composed of contributions to all excited states in the target nucleus ^{64}Zn with excitation energies E_x below $E_{\mathrm{c.m.}}$ of the scattering experiment. In practice, the spectra in Fig. 1 allow a determination of the

(α,α') cross section only for the lowest excited states in ^{64}Zn, and in particular at backward angles a significant yield appears about 5 MeV below the elastic peak. In addition to inelastic scattering from ^{64}Zn, this yield may also come from reaction products of α-induced reaction on the ^{64}Zn target and all target contaminations because the detectors do not allow the identification of the ejectiles. Furthermore, the measurement of each angular distribution is complicated because inelastic peaks may overlap with elastic scattering from lighter nuclei in the target (e.g., in the carbon backing). In addition, at forward angles the (α,α') cross section is much smaller than the elastic cross section which approaches the Rutherford cross section and thus increases dramatically to small scattering angles with with $1/\sin^4(\vartheta/2)$.

1. Inelastic scattering to low-lying excited states

The first excited states in the level scheme of ^{64}Zn consist of a 2^+ state at 992 keV and a triplet of states (0^+, 2^+, 4^+) with almost twice the excitation energy of the first 2^+ state, i.e., a typical vibrational behavior. Thus, these inelastic angular distributions were analyzed within the anharmonic vibrator model which is implemented in the widely used coupled-channels ECIS code [74].

Experimental angular distributions were measured for the first 2^+ state at 992 keV and the 4^+ state at 2307 keV. The experimental resolution was not sufficient to separate the second 2^+ state at 1799 keV and the 0^+ state at 1910 keV; only the sum of both states could be determined. For experimental details, see Sec. II A.

It has been difficult to fit the elastic scattering angular distributions; see Sec. III B. Obviously, these problems appear also when simultaneous fits are made to elastic and inelastic angular distributions. Several fits with different potentials and a varying number of adjustable parameters were made. These fits show significant differences in the reproduction of the angular distributions, but fortunately the angle-integrated inelastic cross sections are quite stable. The results are shown in Fig. 10 for the 12.1-MeV data and in Fig. 11 for the 16.1-MeV data.

As a first approximation, the widely used potential of McFadden and Satchler [11] was applied in combination with an adjustment of the couplings to the inelastic states (dotted lines in Figs. 10 and 11). The reproduction of the elastic angular distributions is reasonable but not perfect. Such a behavior is expected because the potential parameters were not readjusted. The angular distribution of the 2_1^+ state is reasonably well described, but the two-phonon states and in particular the 4^+ state cannot be reproduced.

In a next step, the Woods-Saxon potential from the optical model fits (restricted to scattering angles below $155°$) was used (dashed lines, labeled "WS close to OM"); see also Sec. III B. Again, the coupling to the inelastic states was fitted, and a minor readjustment was allowed for the depths of the real and imaginary parts of the Woods-Saxon potential. Of course, from the fitting procedure the agreement for the elastic angular distribution improves. But simultaneously also the description of the inelastic angular distributions improves.

In a third calculation, additionally all parameters of the Woods-Saxon potentials (real and imaginary depths, radii, and
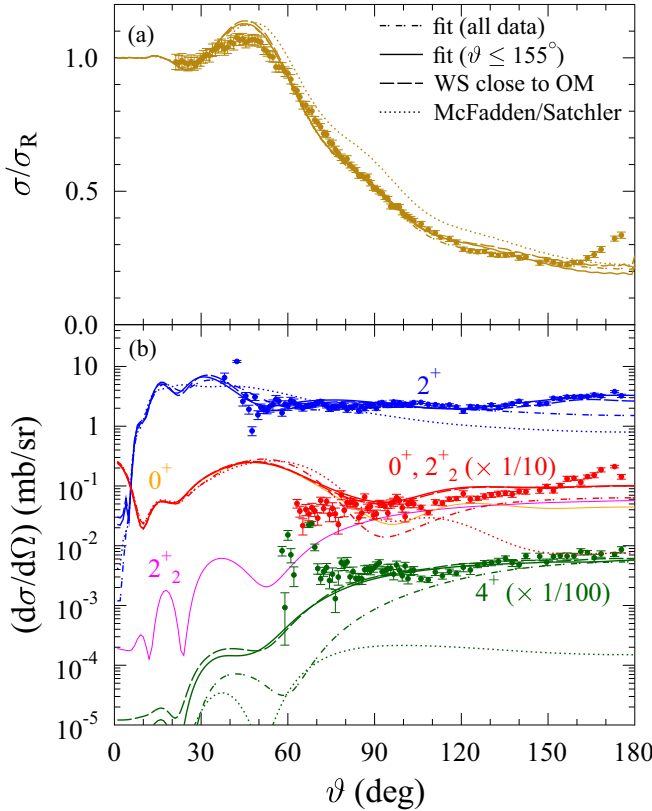
FIG. 10. Inelastic ^{64}Zn$(\alpha,\alpha')^{64}$Zn scattering cross sections at the energy 12.1 MeV: (a) the elastic angular distribution (normalized to Rutherford) and (b) the inelastic angular distributions for the first 2^+ state (blue), the sum of 0^+ and 2_2^+ (red), and the 4^+ state (green). In addition, for the best-fit calculation (solid lines) a decomposition into the 0^+ (orange) and 2_2^+ states (magenta) is shown. For explanation of the various calculations, see text.

FIG. 11. Inelastic ^{64}Zn$(\alpha,\alpha')^{64}$Zn scattering cross section at the energy 16.1 MeV. For explanations, see Fig. 10.

diffuseness) were adjusted simultaneously [solid lines, labeled "fit ($\vartheta \leqslant 155°$)"]. Although a smaller χ^2 is obtained, the visible changes in the angular distributions remain relatively small.

The final calculation repeats the third calculation, but it includes all experimental data, i.e., including the backward rise of the elastic angular distributions beyond $\vartheta \approx 155°$. The results [dash-dotted lines, labeled "fit (all data)"] show significantly worse agreement in the backward angular region of the inelastic angular distributions. This is related to a wide variation of the WS parameters, similar to the problems found in the OM study in Sec. III B. Hence, the backward rise of the elastic cross sections cannot be explained by the inelastic coupling to low-lying excited states.

Interestingly, despite the relatively wide changes of the inelastic angular distributions, the angle-integrated inelastic cross sections remain relatively stable. For example, at 12.1 MeV for the dominating first 2^+ state a cross section of 27.3 mb is obtained from the McFadden-Satchler potential, the Woods-Saxon potential from the optical model fit gives 32.9 mb, and the fits to data up to 155° (all data) result in 34.3 mb (30.1 mb). Excluding the McFadden-Satchler result (without any adjustment of the potential to the experimental
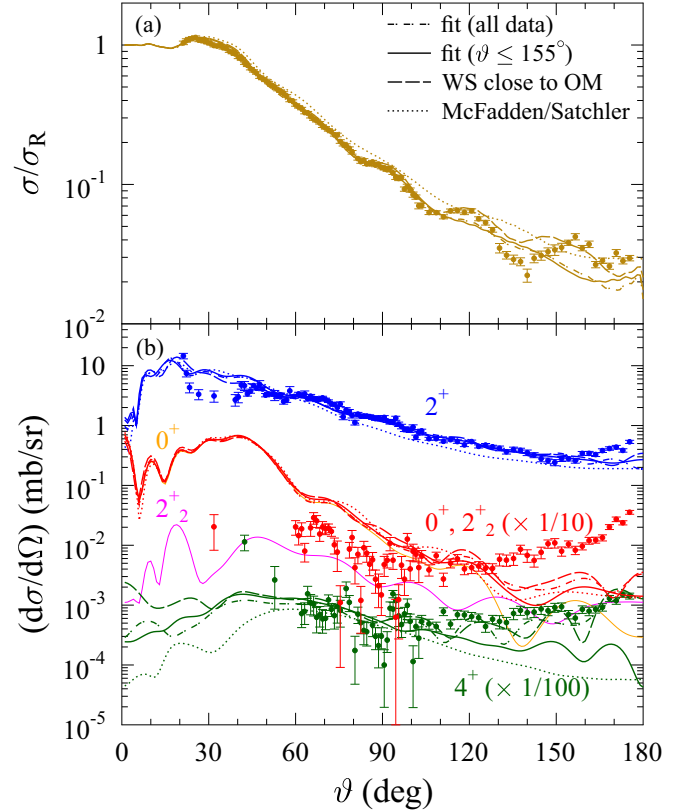
data), we adopt a semi-experimental angle-integrated cross section of 33 ± 3 mb in this case. Similar results are found for all angle-integrated inelastic cross sections at both experimental energies. The results are listed in Table III. For each level, the given uncertainties are estimated from the variations of the different fits. However, it should be kept in mind that the experimental inelastic angular distributions do not cover the full angular range and thus cannot fully constrain the fits; this holds in particular for the significant contribution of the 0_2^+ state at forward angles. Therefore, a somewhat increased uncertainty of about 15% is carefully estimated for the sum over the experimentally determined inelastic cross sections to low-lying excited states in Table III.

2. Inelastic scattering to higher-lying excited states

The inelastic (α,α') cross sections to higher-lying states above the $(0^+, 2^+, 4^+)$ triplet were estimated using the combination of direct and compound contributions as implemented in the widely used nuclear reaction code TALYS (version 1.8). Contrary to the first excited states with their dominating direct contributions, inelastic scattering to higher-lying states is dominated by compound contributions. In these TALYS calculations 30 low-lying levels below $E^* = 3.5$ MeV in ^{64}Zn were taken into account explicitly; for $E^* > 3.5$ MeV a continuum contribution is estimated using a theoretical level density.

The first four excited states were already taken into account in Sec. III E 1. Thus, the summed inelastic cross section to

TABLE III. Angle-integrated inelastic cross sections (in mb).

E_α	$E_{\mathrm{c.m.}}^{\mathrm{eff.}}$	2_1^+ (992 keV)	2_2^+ (1799 keV)	0_2^+ (1910 keV)	4_1^+ (2307 keV)	$\Sigma_{\mathrm{low}}^{\mathrm{expt}}$	$\Sigma_{\mathrm{high}}^{\mathrm{calc}}$
12.05	11.29 ± 0.09	33 ± 3	3.1 ± 0.5	10.2 ± 0.5	3.2 ± 0.5	$49.5 \pm 7.5^{\mathrm{a}}$	$31.5 \pm 6.3^{\mathrm{b}}$
16.12	15.17 ± 0.08	28 ± 1	0.6 ± 0.2	13.6 ± 0.5	0.9 ± 0.1	$43.1 \pm 6.5^{\mathrm{a}}$	$157.9 \pm 30.6^{\mathrm{b}}$

[a]Discussion of uncertainty: see text.
[b]Estimated uncertainty of 20% (see text).

higher-lying states $\sum_{\mathrm{high}}$ is estimated from the calculated total inelastic cross section in TALYS minus the calculated inelastic cross sections to the first four excited states. Fortunately, even a broad variation of the TALYS parameters (mainly a variation of the α-nucleus potential) leads to relatively stable values for the inelastic cross sections. At the lower energy of 12.1 MeV, $\sum_{\mathrm{high}}$ varies between 26.6 and 34.3 mb with an average value of 31.5 ± 2.8 mb. Because of the missing experimental constraint, we finally assign a larger 20% uncertainty to this value. At the higher energy of 16.1 MeV, $\sum_{\mathrm{high}}$ shows significantly larger values between 139 and 168 mb with an average of 157.9 ± 11.1 mb. Again, we finally assign a 20% uncertainty (see Table III). Indeed, this choice of the uncertainty for $\sum_{\mathrm{high}}$ is somewhat arbitrary. But we think that increasing the TALYS uncertainties by a factor of about 2 should provide a careful estimate of the real uncertainty of $\sum_{\mathrm{high}}$.

F. Compound-elastic contributions to low-lying states

In general, the compound mechanism may also contribute to the elastic angular distribution and to the inelastic angular distributions of the low-lying states. The angle-integrated compound-elastic contribution is small with about 5–7 mb at 12.1 MeV and around 0.5 mb at 16.1 MeV. Angle-integrated compound-inelastic cross sections to the low-lying states in Sec. III E 1 are of the order of a few millibarns at 12.1 MeV and below 1 mb at 16.1 MeV (calculated by TALYS, again mainly varying the α-nucleus potential). Thus, the compound contributions may slightly affect the elastic angular distribution in particular at backward angles where the direct cross section is small, and they may also contribute to the unexpected elastic cross sections at backward angles (see Sec. III D). The inelastic angular distributions will also be somewhat affected by the compound contributions; however, as long as a reasonable description of the experimental angular distributions is achieved within the direct coupled-channels model, the angle-integrated inelastic cross section should be well defined by these calculations in the coupled-channels approach (as done in Sec. III E 1).

IV. COMPARISON OF TOTAL CROSS SECTIONS FROM ELASTIC SCATTERING TO REACTION CROSS SECTIONS

The total nonelastic cross section σ_{reac} is given by the sum over all open channels. For ^{64}Zn at the energies under study this means

$$
\begin{aligned}
\sigma_{\mathrm{reac}} = {} & \sigma(\alpha,\alpha') + \sigma(\alpha,\gamma) + \sigma(\alpha,n) + \sigma(\alpha,p) \\
& + \sigma(\alpha,\alpha p) + \sigma(\alpha,\alpha n) + \sigma(\alpha,2\alpha) + \sigma(\alpha,2p) \\
& + \sigma(\alpha,d) + \sigma(\alpha,t) + \sigma(\alpha,{}^3\mathrm{He}).
\end{aligned} \tag{8}
$$

σ_{reac} in the above Eq. (8) can be derived from Eq. (5), i.e.. from the angular distribution of elastic scattering (see Sec. III B and Table II). The determination of the sum on the right-hand side of Eq. (8) is discussed in detail below.

The identity of σ_{reac} from elastic scattering in Eq. (5) and from the sum over nonelastic channels in Eq. (8) follows directly from basic quantum mechanics. In our previous work [37] we calculated the ratio r between the result from elastic scattering and the sum over the nonelastic channels, and $r = 1$ was found within the experimental uncertainties. As there is no reason to question this theoretically expected ratio of $r \equiv 1$, we can also reverse the arguments: fixing σ_{reac} from Eq. (5) allows one to obtain experimental constraints for the cross sections of unobserved nonelastic channels in the sum on the right-hand side of Eq. (8). This will become important in particular for the compound-inelastic (α,α') cross section at the higher energy of 16.1 MeV.

At the lower energy of 12.1 MeV, all channels with two outgoing particles in the third line of Eq. (8) were neglected because these channels are either closed or have negligible cross sections. The same holds for the last line in Eq. (8). The remaining contributions can be taken almost completely from experiment. The cross sections of the (α,γ), (α,n), and (α,p) reactions in the second line of Eq. (8) are taken from Table I; their sum amounts to 366 ± 40 mb. The (α,α') inelastic scattering cross section is taken from experiment for the low-lying excited states with 49.5 ± 7.5 mb and from theoretical estimates for the higher-lying states with 31.5 ± 6.3 mb (see Table III). Summing up all these values leads to a total nonelastic cross section of 447 ± 41 mb. Within the uncertainties, this result is in excellent agreement with the value of 428 ± 7 mb derived from elastic scattering (see Table II). As expected, the ratio r between the result from elastic scattering and the sum over the contributing channels results in $r = 0.957 \pm 0.090$, i.e., it is identical to unity within the uncertainties. Compared to our previous study [37], the uncertainty of the ratio r could be reduced by a factor of 2. This reduction is based on improved scattering data at the same energy of the reaction cross sections. Note that the sum in Eq. (8) is based on experimental data with the only exception of inelastic scattering to higher-lying states in ^{64}Zn which contributes only with 31.5 mb (or 7%) to the sum of 447 mb.

At the higher energy of 16.1 MeV the situation is somewhat more complicated because more channels are open. Nevertheless, because of strongly negative Q values, the cross sections of the (α,d) and $(\alpha,{}^3\mathrm{He})$ reactions remain negligibly small, and the (α,t) channel is still closed; thus, the fourth line in Eq. (8) still can be neglected. The same holds for the reactions with two outgoing particles in the third line of Eq. (8) with the exception of the $(\alpha,2p)$ reaction. According to TALYS calculations, this

TABLE IV. Predictions of σ_{reac} from various global α-nucleus potentials, compared to the results from elastic scattering. All cross sections are given in millibarns.

$E_\alpha = 12.05$ MeV	$E_\alpha = 16.12$ MeV	Reference
428 ± 7	905 ± 18	Experiment (this work)
408	833	Watanabe [75]
376	809	McFadden and Satchler [11]
427	868	Demetriou *et al.*, V1 [31]
405	837	Demetriou *et al.*, V2 [31]
455	845	Demetriou *et al.*, V3 [31]
415	857	Avrigeanu *et al.* [29]
475	915	ATOMKI-V1 [9]
552	1010	Su and Han [27]

reaction contributes with 17.6–18.4 mb. Because there is no experimental constraint, we estimate a contribution of 18 mb with an uncertainty of 25%. The other contributions are determined in the same way as for the lower energy of 12.1 MeV. The sum of the (α,γ), (α,n), and (α,p) cross sections amounts to 668 ± 72 mb. The (α,α') inelastic scattering cross section is composed of the experimental result for the low-lying excited states (43.1 ± 6.5 mb) and of the theoretical estimates for the higher-lying states (157.9 ± 30.6 mb). The sum of 887 ± 79 mb again agrees well with the result of 905 ± 18 mb from elastic scattering, leading to a ratio of $r = 1.020 \pm 0.093$ between the result from elastic scattering and the sum over the reaction channels.

As pointed out above, the expected ratio $r \equiv 1.0$ allows one to constrain the cross sections of unobserved nonelastic channels. For the data at the higher energy of 16.1 MeV this leads to the conclusion that the significant contribution of compound-inelastic scattering to higher-lying excites states of 158 ± 31 mb is indeed confirmed experimentally by the present data. Starting from the experimental result from elastic scattering in Eq. (5) and subtracting the experimentally determined cross sections, i.e., the inelastic scattering to low-lying states and the reaction channels in the second line of Eq. (8), this leads to a remaining cross section of 194 ± 75 mb, which has to be distributed among the remaining open channels which are mainly inelastic scattering to higher-lying states (≈ 158 mb from TALYS) and to a minor degree the $(\alpha,2p)$ reaction (≈ 18 mb from TALYS).

V. PREDICTIONS FROM GLOBAL α-NUCLEUS POTENTIALS

Finally, the experimental results for the total reaction cross sections σ_{reac} and for the (α,γ), (α,n), and (α,p) cross sections are compared to predictions from global α-nucleus potentials. Interestingly, it turns out that the widely used α-nucleus potentials predict very similar total cross sections. The predictions of Watanabe (TALYS default) [75], McFadden and Satchler [11], Demetriou *et al.* [31], Avrigeanu *et al.* [29], Su and Han [27], and from the ATOMKI-V1 potential [9] are listed in Table IV. The new potential by Su and Han [27] overestimates the total reaction cross section in particular at low energies; at 5 MeV the predicted σ_{reac} from the potential
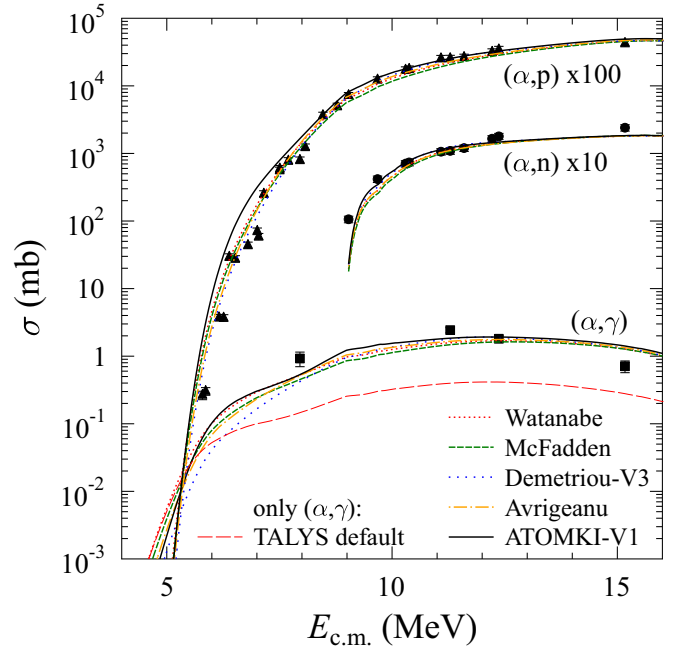

FIG. 12. Cross sections of the ^{64}Zn$(\alpha,\gamma)^{68}$Ge, ^{64}Zn$(\alpha,n)^{67}$Ge, and ^{64}Zn$(\alpha,p)^{67}$Ga reactions. The experimental data are taken from our previous work [37] except the new results at the highest energy $E_\alpha = 16.1$. The calculations are based on different global α-nucleus optical potentials [9,11,29,31,75]. For better readability, two versions of [31] have been omitted. The differences between the predictions from various α-nucleus potentials are relatively small. TALYS default parameters have been used in general except for the γ-ray strength function; the default γ-ray strength underestimates the (α,γ) cross section (thin red long-dashed line). For further discussion see text.

by Su and Han is about 11 μb whereas the predictions from the other potentials [9,11,29,31,75] vary between 0.3 and 1.6 μb with a mean value of about 0.8 μb. (For completeness it may be noted here that the present TALYS 1.8 version uses still the Watanabe potential as a default, although the TALYS manual states that this has changed to Avrigeanu *et al.* [29].)

The total reaction cross section σ_{reac} is mainly composed of the dominating (α,p) and (α,n) channels. The branching between these two channels is sensitive to the chosen nucleon potential whereas the total reaction cross section σ_{reac} is sensitive only to the α-nucleus potential. The TALYS default option for the nucleon potential [76] works very well here and was not changed in this work. Excellent agreement for the (α,n) and (α,p) cross sections is found; see Fig. 12.

The cross section of the ^{64}Zn$(\alpha,\gamma)^{68}$Ge reaction is sensitive to the α-nucleus potential and to the γ-ray strength function. Here the best result is obtained using the Hartree-Fock BCS γ-ray strength from [77]. The TALYS default option using generalized Lorentzian γ-ray strength from [78] significantly underestimates the ^{64}Zn$(\alpha,\gamma)^{68}$Ge cross section (see Fig. 12, thin red long-dashed line).

VI. SUMMARY AND CONCLUSIONS

Elastic and inelastic ^{64}Zn$(\alpha,\alpha)^{64}$Zn scattering was measured at the energies of 12.1 and 16.1 MeV. At the same

energies the cross sections of the (α,γ), (α,n), and (α,p) reactions were determined using the activation technique. The experimental angular distributions of elastic scattering cover the full angular range and thus allow for a precise determination of the total nonelastic reaction cross section $\sigma_{\rm reac}$ with uncertainties of about 2–3%. A perfect description of the elastic angular distributions could only be achieved using phase shift fits. The surprising rise of the elastic cross sections at very backward angles may be considered as so-called ALAS and could not be fully explained. Fortunately, the behavior of the angular distributions at these very backward angles practically does not affect the determination of the total cross sections $\sigma_{\rm reac}$.

The total reaction cross sections follow a general smooth trend when presented as so-called reduced cross sections $\sigma_{\rm red}$ versus reduced energies $E_{\rm red}$. The data for ^{64}Zn lie in between the common behavior for heavy target nuclei with $A \gtrsim 90$ [9] and slightly increased values for lighter target nuclei with $A \lesssim 50$ [26].

The total nonelastic reaction cross section was also determined from the sum over the cross sections of all nonelastic channels (including inelastic scattering). At the lower energy of 12.1 MeV excellent agreement between $\sigma_{\rm reac}$ from elastic scattering and from the sum over nonelastic channels was found; here almost all open channels (including inelastic scattering to low-lying states in ^{64}Zn) could be determined experimentally. At the higher energy of 16.1 MeV we find again excellent agreement for $\sigma_{\rm reac}$ from the two approaches. However, now a significant contribution of inelastic scattering to higher-lying states in ^{64}Zn is required which is indeed predicted in the statistical model. In turn, this may be

considered as an experimental verification of these statistical model predictions. Compared to our previous work [37], the experimental uncertainties in the comparison of $\sigma_{\rm reac}$ from the two approaches could be reduced significantly by about a factor of 2.

Usually, the cross sections of α-induced reactions in the statistical model depend sensitively on the chosen α-nucleus potential. At 12.1 and 16.1 MeV, the recent global α-nucleus potentials predict very similar total reaction cross sections $\sigma_{\rm reac}$, and with the exception of the latest potential by Su and Han [27] this behavior surprisingly persists down to lower energies. Thus, in the case of ^{64}Zn the total reaction cross section $\sigma_{\rm reac}$ can be described well, and the (α,γ), (α,n), and (α,p) data can be used to constrain further ingredients of the statistical model. In particular, it is found that the TALYS default nucleon optical potential [76] works very well, whereas the (α,γ) data can be best described using the Hartree-Fock BCS γ-ray strength [77] but the default generalized Lorentzian [78] significantly underestimates the experimental data.

[1] S. E. Woosley and W. M. Howard, Astrophys. J. Suppl. **36**, 285 (1978).
[2] M. Arnould and S. Goriely, Phys. Rep. **384**, 1 (2003).
[3] T. Rauscher, Phys. Rev. C **73**, 015804 (2006).
[4] W. Rapp *et al.*, Astrophys. J. **653**, 474 (2006).
[5] P. Mohr, Zs. Fülöp, and H. Utsunomiya, Eur. Phys. J. A **32**, 357 (2007).
[6] T. Rauscher, Int. J. Mod. Phys. E **20**, 1071 (2011).
[7] T. Rauscher, P. Mohr, I. Dillmann, and R. Plag, Astrophys. J. **738**, 143 (2011).
[8] T. Rauscher, Phys. Rev. C **88**, 035803 (2013).
[9] P. Mohr, G. G. Kiss, Zs. Fülöp, D. Galaviz, Gy. Gyürky, and E. Somorjai, At. Data Nucl. Data Tables **99**, 651 (2013).
[10] A. Palumbo *et al.*, Phys. Rev. C **85**, 035808 (2012); **88**, 039902(E) (2013).
[11] L. McFadden and G. R. Satchler, Nucl. Phys. **84**, 177 (1966).
[12] E. Somorjai *et al.*, Astron. Astrophys. **333**, 1112 (1998).
[13] Gy. Gyürky *et al.*, Phys. Rev. C **74**, 025805 (2006).
[14] N. Özkan *et al.*, Phys. Rev. C **75**, 025801 (2007).
[15] I. Cata-Danil *et al.*, Phys. Rev. C **78**, 035803 (2008).
[16] C. Yalçın *et al.*, Phys. Rev. C **79**, 065801 (2009).
[17] Gy. Gyürky *et al.*, J. Phys. G **37**, 115201 (2010).
[18] G. G. Kiss *et al.*, Phys. Lett. B **695**, 419 (2011).
[19] M. Avrigeanu and V. Avrigeanu, Phys. Rev. C **82**, 014606 (2010).
[20] A. Sauerwein *et al.*, Phys. Rev. C **84**, 045808 (2011).
[21] P. Mohr, Phys. Rev. C **84**, 055803 (2011).
[22] A. Palumbo, W. P. Tan, J. Görres, M. Wieschler, N. Özkan, R. T. Güray, and C. Yalçın, Phys. Rev. C **85**, 028801 (2012).
[23] S. J. Quinn *et al.*, Phys. Rev. C **89**, 054611 (2014).
[24] S. J. Quinn *et al.*, Phys. Rev. C **92**, 045805 (2015).
[25] P. Scholz, F. Heim, J. Mayer, C. Münker, L. Netterdon, F. Wombacher, and A. Zilges, Phys. Lett. B **761**, 247 (2016).
[26] P. Mohr, Europ. Phys. J. A **51**, 56 (2015).
[27] X.-W. Su and Y.-L. Han, Int. J. Mod. Phys. E **24**, 1550092 (2015).
[28] V. Avrigeanu and M. Avrigeanu, Phys. Rev. C **91**, 064611 (2015).
[29] V. Avrigeanu, M. Avrigeanu, and C. Mănăilescu, Phys. Rev. C **90**, 044612 (2014).
[30] P. Demetriou, A. Lagoyannis, A. Spyrou, H. W. Becker, T. Konstantinopoulos, M. Axiotis, and S. Harissopulos, AIP Conf. Proc. **1090**, 293 (2009).
[31] P. Demetriou, C. Grama, and S. Goriely, Nucl. Phys. A **707**, 253 (2002).
[32] J. Pereira and F. Montes, Phys. Rev. C **93**, 034611 (2016).
[33] V. Avrigeanu and M. Avrigeanu, Phys. Rev. C **94**, 024621 (2016).
[34] Peter Mohr, Phys. Rev. C **94**, 035801 (2016).
[35] T. Rauscher, Phys. Rev. Lett. **111**, 061104 (2013).
[36] V. Avrigeanu, M. Avrigeanu, and C. Mănăilescu, arXiv:1605.05455.

[37] Gy. Gyürky, P. Mohr, Zs. Fülöp, Z. Halász, G. G. Kiss, T. Szücs, and E. Somorjai, Phys. Rev. C **86**, 041601(R) (2012).

[38] Database ENDSF, version April 26, 2016; available online at www.nndc.bnl.gov/ensdf, based on [39].

[39] B. Singh, Nucl. Data Sheets **108**, 197 (2007).

[40] EXFOR database, http://www-nds.iaea.org/exfor.

[41] P. Mohr, Phys. Rev. C **87**, 035802 (2013).

[42] A. Di Pietro *et al.*, Phys. Rev. C **69**, 044613 (2004).

[43] T. B. Robinson and V. R. W. Edwards, Nucl. Phys. A **301**, 36 (1978).

[44] C. B. Fulmer, J. Benveniste, and A. C. Mitchell, Phys. Rev. **165**, 1218 (1968).

[45] J. B. A. England *et al.*, Nucl. Phys. A **388**, 573 (1982).

[46] F. Ballester, E. Casal, and J. B. A. England, Nucl. Phys. A **490**, 245 (1988).

[47] K. B. Baktybaev, A. D. Dujsebaev, and A. B. Kabulov, J. Izv. Ros. Akad. Nauk, Ser. Fiz. **39**, 2152 (1975) [Bull. Russ. Acad. Sci. Phys. **39**, 123 (1975)].

[48] S. Ya. Aisina, K. A. Kuterbekov, N. N. Pavlova, and A. V. Yushkov, J. Izv. Ros. Akad. Nauk, Ser. Fiz. **53**, 37 (1989).

[49] N. Alpert, J. Alster, and E. J. Martens, Phys. Rev. C **2**, 974 (1970).

[50] D. K. McDaniels, J. S. Blair, S. W. Chen, and G. W. Farwell, Nucl. Phys. **17**, 614 (1960).

[51] H. W. Broek, T. H. Braid, J. L. Yntema, and B. Zeidman, Nucl. Phys. **38**, 305 (1962).

[52] C. Pirart, M. Bosman, P. Leleux, P. Macq, and J. P. Meulders, Phys. Rev. C **17**, 810 (1978).

[53] P. Mohr, D. Galaviz, Zs. Fülöp, Gy. Gyürky, G. G. Kiss, and E. Somorjai, Phys. Rev. C **82**, 047601 (2010).

[54] V. Chisté, R. Lichtenthäler, A. C. C. Villari, and L. C. Gomes, Phys. Rev. C **54**, 784 (1996).

[55] P. R. S. Gomes, J. Lubian, I. Padron, and R. M. Anjos, Phys. Rev. C **71**, 017601 (2005).

[56] S. Almarez-Calderon *et al.*, Phys. Rev. Lett. **112**, 152701 (2014).

[57] M. Bowers, Y. Kashiv, W. Bauder, M. Beard, P. Collon, W. Lu, K. Ostdiek, and D. Robertson, Phys. Rev. C **88**, 065802 (2013).

[58] P. Mohr, Phys. Rev. C **89**, 058801 (2014).

[59] A. M. Howard, M. Munch, H. O. U. Fynbo, O. S. Kirsebom, K. L. Laursen, C. A. Diget, and N. J. Hubbard, Phys. Rev. Lett. **115**, 052701 (2015).

[60] J. R. Tomlinson *et al.*, Phys. Rev. Lett. **115**, 052702 (2015).

[61] S. Almarez-Calderon *et al.*, Phys. Rev. Lett. **115**, 179901(E) (2015); erratum to [56].

[62] P. Mohr, Proceedings of Nuclear Physics in Astrophysics VII, York, UK, 18-22 May 2015, J. Phys. Conf. Ser. (in press), arXiv:1608.08233 (2015).

[63] G. G. Kiss *et al.*, Phys. Rev. C **88**, 045804 (2013).

[64] K. Langanke, Nucl. Phys. A **377**, 53 (1982).

[65] F. Michel, G. Reidemeister, and Y. Kondo, Phys. Rev. C **51**, 3290 (1995).

[66] H. Abele and G. Staudt, Phys. Rev. C **47**, 742 (1993).

[67] U. Atzrott, P. Mohr, H. Abele, C. Hillenmayer, and G. Staudt, Phys. Rev. C **53**, 1336 (1996).

[68] Y. Hirabayashi and S. Ohkubo, Phys. Rev. C **88**, 014314 (2013).

[69] M. N. A. Abdullah *et al.*, Phys. Lett. B **571**, 45 (2003).

[70] D. Bachelier, M. Bernas, J. L. Boyard, H. L. Harney, J. C. Jourdain, P. Radvanyi, and M. Roy-Stephan, Nucl. Phys. A **195**, 361 (1972).

[71] C. Samanta, S. Ghosh, M. Lahiri, S. Ray, and S. R. Banerjee, Phys. Rev. C **45**, 1757 (1992).

[72] Yong-Yu Yang, Hai-Lan Tan, and Qing-Run Li, Commun. Theor. Phys. **55**, 655 (2011).

[73] J. W. Frickey, K. A. Eberhard, and R. H. Davis, Phys. Rev. C **4**, 434 (1971).

[74] J. Raynal, Saclay Report No. CEA-N-2772, 1994 (unpublished).

[75] S. Watanabe, Nucl. Phys. **8**, 484 (1958).

[76] A. J. Koning and J. P. Delaroche, Nucl. Phys. A **713**, 231 (2003).

[77] R. Capote *et al.*, Nucl. Data Sheets **110**, 3107 (2009).

[78] J. Kopecky and M. Uhl, Phys. Rev. C **41**, 1941 (1990).